RESEARCH PAPER

Finite element analysis of residual stress in hybrid laser-arc welding for butt joint of 12 mm-thick steel plate

Guoxiang Xu[1] · Haichao Pan[1] · Peng Liu[1] · Pengfei Li[1] · Qingxian Hu[1] · Baoshuai Du[2]

Abstract

As a high-efficiency and high-quality welding process, hybrid laser-arc welding (HLAW) has significant potential of application in welding thick plate. Understanding the features of welding residual stress benefits the optimization of HLAW process. In the present study, based on thermal elastic–plastic theory, a three-dimensional finite element model is developed to predict the residual stress and distortion in HLAW for butt joint of 12-mm-thick steel plate. GMAW heat input and laser energy are modeled as one double-ellipsoid body heat source and one cone body heat source with enhanced peak density along the central axis, respectively. Residual stresses and distortions are calculated for single-pass and multi-pass hybrid welding processes. The results show that the distribution features of longitudinal and von Mises equivalent residual stresses in single-pass hybrid welding are similar to that in multi-pass hybrid welding. A large tensile stress is generated at the weld zone and its vicinity. Compared with GMAW, the zone with high residual stress in hybrid welding is decreased largely, but there is no improvement in peak residual stress. Among three cases, the distortion in single-pass hybrid welding has the lowest value.

Keywords Hybrid welding · Thick plate · Finite element model · Residual stress · Distortion

1 Introduction

Butt-welded structure of medium-thick steel plate (more than 10 mm in thickness) is widely used in fabrication and manufacturing industries. High-quality and high-efficiency welding of thick plate has been an urgent requirement in these fields. As a hybrid welding process, hybrid laser-arc welding (HLAW) combines the merits of the two welding processes and compensates deficiencies of each component. As reviewed by Staufer [1] and Defalco [2], the most relevant benefits of this technology reported are an increase in the welding speed, the weldable thickness, the gap bridging ability, and the weld quality. Thus, HLAW has received a growing attention in heavy industries and is also finding its application

✉ Guoxiang Xu
   xugxiang@163.com

[1] Jiangsu University of Science and Technology, Zhenjiang 212003, China

[2] Shandong Electric Power Research Institute, Jinan 250002, China

in joining of thick plate [3]. However, for welded structure, one of the major problems is the welding-induced residual stress and distortion due to local transient heating and cooling [4]. In the case of thick plate, this problem is more serious. Therefore, it is of significance to deeply study the residual stress and distortion in HLAW for further expanding its application.

Up to date, extensive experimental and simulation studies have been conducted on the hybrid welding, including weld formation [5–7], thermal field, and fluid flow [8–12] in the weld pool. However, few works involved the residual stress and deformation in hybrid welding. Wahha et al. [3] proposed an innovative HLAW technology to achieve single-pass welding of 25-mm thick steel. Cho et al. [8, 9] developed a three-dimensional model to study the basic fluid flow pattern of molten pool in hybrid bead-on-plate welding. Zhou and Tsai [10] numerically investigated the interaction between the droplet and weld pool in spot hybrid welding. Xu et al. [11] explained the suppression of bead hump in hybrid bead-on-plate welding in terms of fluid flow according to the simulated results.

Due to experimental limitation, welding residual stress and distortion are investigated by mainly using the numerical simulation technique [4, 13]. For HLAW, only few literatures

reported this aspect currently. Zhang et al. [14] developed a three-dimensional finite element model to analyze the residual stress and distortion in HLAW and found that a large tensile longitudinal stress was generated in and near the weld zone and under the condition of the same weld penetration, the peak stress in GMAW was 28% higher than that of hybrid welding. However, their results were only limited to bead-on-plate welding of 9-mm thick steel. Hee et al. [15] predicted the residual stress in hybrid welding of 13-mm thick steel plate using a two-dimensional model without considering the weld reinforcement. Different from those of Zhang et al. [14], their computed results indicated that the peak value of longitudinal residual stress occurred in heat-affected zone (HAZ). Kong et al. [16] calculated the residual stress in single-pass hybrid welding of 6-mm thick steel. But the study results showed that a great compressive longitudinal stress was located at and around the fusion zone, which is not consistent with those of Zhang et al. [14] and Hee et al. [15]. In addition, Xu et al. [17] numerically studied the residual stress and distortion in hybrid T-welded joint of 2-mm thick aluminum alloy. According to the above analysis, it is found that most of these previous efforts were focused on relatively thin plate (less than 10 mm in thickness). Besides, owing to difference in the calculation condition, the conclusions on residual stress distribution feature in hybrid welding are still unclear and are even in debate in some aspects. The previous study results are not suitable to the hybrid welding of thick-section steel. Consequently, there is still a lack of deep understanding of residual stress and distortion in hybrid welding for butt joint of thick plate currently.

In this study, a three-dimensional thermomechanical finite element model is developed to predict the welding-induced residual stress and deformation in HLAW for butt joint of 12-mm-thick Q460 steel plate. The characteristics of residual stress distribution and distortion are numerically analyzed and are compared with those in GMAW.

2 Experimental procedures

The material used in this study is Q460 ultra-grained steel plate with dimensions of 150 mm × 150 mm × 12 mm. The filler material is ER55-G with a 1.2-mm diameter. Table 1 gives the chemical composition for base metal and welding wire. Hybrid welding was conducted using a constant wave IPG YLS600 fiber laser with a maximum power of 6 kW and a TPS400 Fronius power source. The fiber laser beam with wavelength of 1.07 μm and focus diameter of 0.7 mm is delivered through a fiber of 400 μm in diameter. The laser welding system has a collimating lens of 150 mm and focusing lens of 200 mm. As illustrated in Fig. 1, in hybrid welding, laser beam was leading and the arc was trailing. The laser beam was perpendicular to the workpiece surface, while the

Table 1 Chemical composition (wt%) of Q460 steel and welding wire

Material	C%	Mn%	Si%	P%	S%	Nb%	Ti%
Q460 (base metal)	0.08	1.29	0.19	0.013	0.004	0.04	–
ER55-G (welding wire)	0.007	1.06	0.58	0.013	0.002	–	0.12

axis of GMAW torch was 27° titled with respect to the centerline of laser beam. The laser-arc distance is 2 mm and shielding gas was Ar80% + $CO_2$20%, which had a flow rate of 20 L/min. Y-groove configuration was used, which was prepared by a heavy-duty milling machine. Single-pass and multi-pass hybrid welding experiments were carried out, which were numbered as case 1 and case 2, respectively. Meanwhile, to compare the residual stress in hybrid welding with that in GMAW, multi-pass GMAW experiment of Q460 steel was also performed, which was numbered as case 3. For GMAW, the welding torch was perpendicular to the workpiece surface. Figure 2 shows the shape and size of grooves of workpieces for hybrid welding and GMAW. Figure 3 presents the weld sequences for three cases. The welding process parameters are listed in Table 2. The blind hole method [18] was used to measure the residual stress on the surface of workpiece. Besides, after welding, cross sections of the weld beads were ground, polished, and etched according to the standard procedures. All these sections were cut midway from the welded specimen. The bead dimensions corresponding to each welding parameter were measured using a stereo microscope.

3 Finite element modeling

The residual stress distribution in HLAW is simulated using a thermal elastic–plastic three-dimensional finite element model. To speed up the calculation process, an uncoupled thermomechanical formulation [4, 14, 16] is adopted in the calculation. For this method, the solution procedure is divided into two steps. First, the transient heat conduction analysis is performed to compute the welding temperature profile and its history, which is independent from the stress analysis. Then, the temperature history obtained at the first step is employed
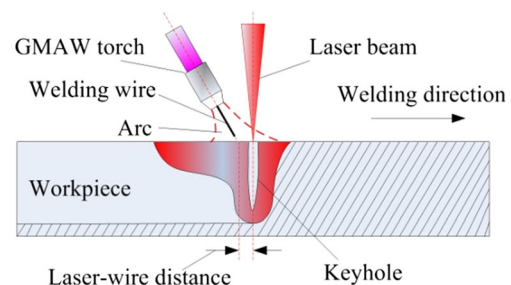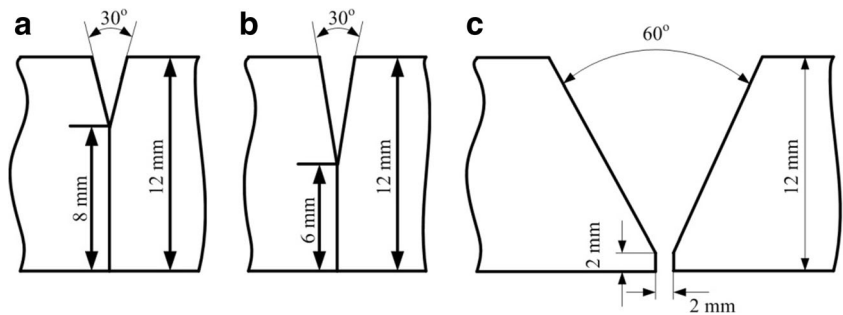

Fig. 1 Schematic of laser + GMAW hybrid welding

as a thermal load in the subsequent mechanical elastic–plastic calculation of the residual stress field. In this study, ANSYS code is used to calculate the welding residual stress and distortion.

3.1 Thermal analysis

3.1.1 Heat source model

For hybrid welding, the total heat input comes from two interacting source terms, i.e., laser power and GMAW energy. In the present study, the energy from GMAW is described using a double-ellipsoid body heat source, which is expressed as follows:

$$q_f = \frac{12\sqrt{3}\eta IU}{\pi\sqrt{\pi}ab_h(c_f + c_r)}\exp\left[-\frac{3x^2}{a^2} - \frac{3y^2}{b_h^2} - \frac{3(z-vt)^2}{c_f^2}\right] z-vt > 0 \tag{1}$$

$$q_r = \frac{12\sqrt{3}\eta IU}{\pi\sqrt{\pi}ab_h(c_f + c_r)}\exp\left[-\frac{3x^2}{a^2} - \frac{3y^2}{b_h^2} - \frac{3(z-vt)^2}{c_r^2}\right] z-vt \leq 0 \tag{2}$$

where q_f and q_r are the heat density functions at the front and rear of heat source center, respectively; I is the welding current, U is the arc voltage, η is the arc efficient, v is the welding speed, t is the time, and a, b_h, c_f, and c_r are the distribution parameters. For GMAW, they are set at 4, 1.6, 3, and 4.5 mm, respectively. For HLAW, owing to compaction of arc by laser beam, a, b_h, c_f, and c_r are set at 3, 1.6, 2.5, and 3.5 mm, respectively.

Considering the weld cross section geometry and heat flux distribution feature along the thickness direction of

workpiece, laser power density is modeled as one cone heat source with the exponentially increased peak density along the central axis. The heat flux function q is expressed as follows [19]:

$$q = Q_0\exp\left[-\frac{\ln(\chi)}{H}y\right]\exp\left[-\frac{3r^2}{r_0^2(y)}\right] \tag{3}$$

$$Q_0 = \frac{3\eta_L P_L\ln(\chi)}{\pi(1-e^{-3})H\left\{r_e^2 - r_i^2\chi - 2\frac{r_i-r_e}{\ln(\chi)}\left[r_e - r_i\chi - \frac{r_i-r_e}{\ln(\chi)}(1-\chi)\right]\right\}} \tag{4}$$

$$r_0(y) = \frac{r_e - r_i}{H}y + r_i \tag{5}$$

where H is the heat source height; r_e and r_i are the radii of heat source top and bottom surfaces, respectively; χ is the proportion coefficient between peak power density at the heat source bottom and the one at top surface, which is set at 1.2; $r_0(y)$ is the function indicating the variation of heat source radius, η_L is the laser thermal efficiency, P_L is the laser power, and Q_0 is the calculation coefficient. In this study, r_e and r_i are set at 1 and 0.5 mm, respectively; H takes 1, 6, and 8 mm at the laser powers of 1.5, 4, and 5.5 kW, respectively.

A combination of the above sub-models for GMAW and laser welding forms the heat source model for HLAW. The coupling of laser beam and electric arc is indirectly considered by appropriately adjusting some distribution parameters according to the experimental weld size [12].

3.1.2 Heat conduction equation

During welding, the fluid flow has a significant effect on heat transfer in weld pool as well as weld geometry, but its
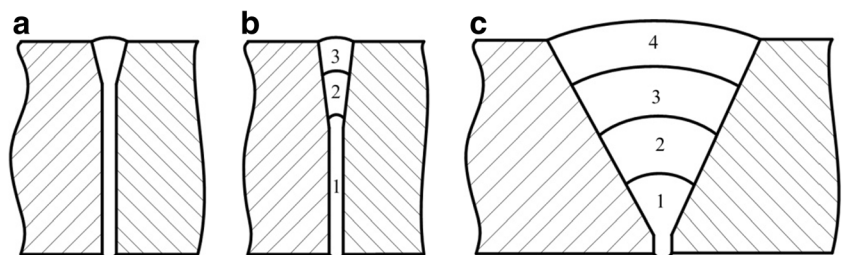
Table 2   The welding process parameters

Case	Weld pass	Laser power (W)	Welding current (A)	Arc voltage (V)	Welding speed (m/min)
Case 1	1	5.5	120	17	0.6
Case 2	1	4.0	100	17	0.6
	2	1.5	120	17	1.0
	3	1.5	120	17	1.0
Case 3	1	–	110	17	0.12
	2	–	120	18	0.12
	3	–	120	18	0.12
	4	–	120	18	0.12

numerical simulation is very complex. To simplify the model, only the thermal conduction in transient state is involved in the calculation and the fluid flow is ignored. The calculation accuracy of weld pool geometry and size is guaranteed by selecting the appropriate heat source model. To consider the effect of fluid flow on temperature field with weld pool, an artificially enhanced thermal conductivity is used at a temperature higher than the melting point of base metal [4]. The heat conduction equation is used in thermal analysis and is expressed as:

$$\rho c \frac{\partial T}{\partial t} = \frac{\partial}{\partial x}\left(k \frac{\partial T}{\partial x}\right) + \frac{\partial}{\partial y}\left(k \frac{\partial T}{\partial y}\right) + \frac{\partial}{\partial z}\left(k \frac{\partial T}{\partial z}\right) + S_H \quad (6)$$

where T is the temperature, ρ is the density, c is the specific heat, k is the thermal conductivity, and S_H is the heat source term, which is the power density of the heat source for hybrid welding.

In this work, the boundary conditions for all the surfaces consider the heat losses due to convection, radiation, and evaporation, which are calculated as:

$$-k \frac{\partial T}{\partial \overrightarrow{n}} = -\alpha_{cr}(T - T_\infty) - m_{er} L_b \quad (7)$$

where $\overrightarrow{n}$ is the normal unit vector to the surface; α_{cr} is the combined heat transfer coefficient due to convection and radiation, m_{er} is the evaporation rate, L_b is the latent heat of evaporation, and T_∞ is the ambient temperature.

Allowing for the computing efficiency and accuracy, a non-uniform grid system is employed in the calculation. A finer grid is applied in and near the weld zone where there is a large stress gradient and the smallest element size is 0.4 mm × 0.4 mm × 1 mm. A coarse grid is designed at the domain far away from the weld bead, shown in Fig. 4. The element "death and birth" technique [16, 20] is utilized to simulate the material filling process in the thermal analysis. Prior to welding, the elements belonging to the weld material are deactivated, which have no effect on the calculation of temperature field (i.e., these elements are "killed"). Then, an empty groove is obtained. With the movement of welding heat source, the elements representing the filler material are reactivated (i.e., the corresponding elements are "born") segment by segment to take into account the influence of filler material on thermal field.

3.2 Mechanical analysis

For low-carbon steel, the changes of material volume and mechanical properties caused by solid-phase transformation have insignificant effect on residual stress compared with thermally induced stress [21]. Therefore, the total strain increment $\Delta\varepsilon$ can only be decomposed into the three components in the following:

$$\Delta\varepsilon = \Delta\varepsilon_e + \Delta\varepsilon_p + \Delta\varepsilon_T \quad (8)$$
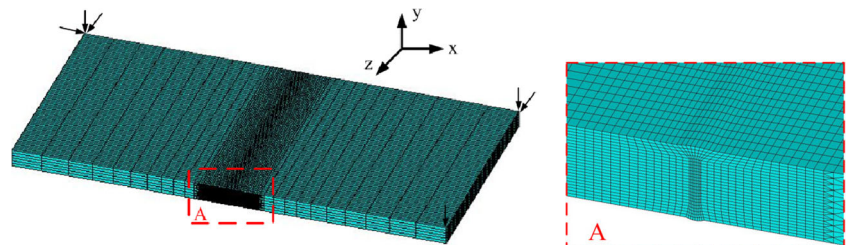
where $\Delta\varepsilon_e$, $\Delta\varepsilon_p$, and $\Delta\varepsilon_T$ are the elastic, plastic, and thermal strain increments, respectively.

In this step, the mesh is the same to that used in the thermal analysis, but the element types need to be transformed to the ones suitable for the structure analysis. Meanwhile, the mechanical constraints are utilized to avoid the rigid body motion of the workpiece, as shown in Fig. 4. The element death and birth method is also employed to consider the effect of filler material on the mechanical analysis of hybrid welding.

3.3 Material properties

The weld metal is assumed to have the same thermal and mechanical properties with the base metal. The temperature-dependent thermal-physical and mechanical properties [22] used in this study are plotted in Figs. 5 and 6, respectively. Other physical properties and parameters [4, 8, 11, 14] are given in Table 3. In the calculation, thermal strain is

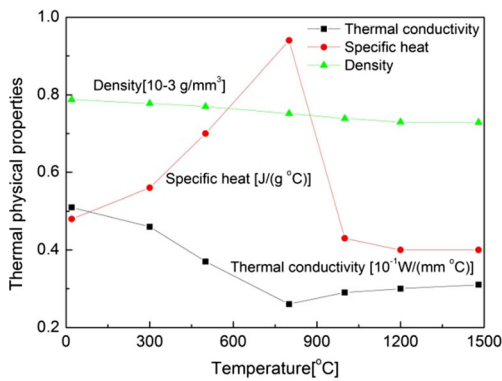**Fig. 4** Finite element mesh of workpiece for single-pass hybrid butt-welding

Fig. 5 Temperature-dependent thermal physical properties [22]

Table 3 Physical properties and other parameters used in calculation [4, 8, 11, 14]

Name	Value
Combined heat transfer coefficient (W/(m² °C))	80
Latent heat of evaporation (J/kg)	6.08×10^6
Enhanced thermal conductivity of liquid metal (W/(m °C))	120
Ambient temperature (°C)	20
Arc thermal efficiency	0.8
Laser thermal efficiency	0.85

considered through thermal expansion coefficient. The elastic behavior of welded material is assumed to satisfy the isotropic Hooke's principle, and the plastic behavior is described by a rate-independent plastic model. The yielding process of the workpiece is simulated based on the von Mises yield criterion, and the strain hardening is taken into account using a bilinear isotropic hardening law.

4 Results and discussion

4.1 Simulated temperature field

Figure 7 compares the calculated shape and size of weld cross section with the experimental results and both are in general agreement, indicating that the developed heat source model can be suitable to calculate the temperature field in welding.

Figure 8 shows the cross-sectional temperature field for the three welding conditions. It is observed that, similar to weld width, the width of the high-temperature region outside weld pool in GMAW is still the greatest among the three cases because of large heat flux distribution zone and low welding speed. However, for single-pass and multi-pass hybrid welding in this study, the former has a relatively wider zone with high temperature outside weld pool due to low welding speed. Figure 9 provides the thermal cycle curves at different locations on the top surface of workpiece for the three cases
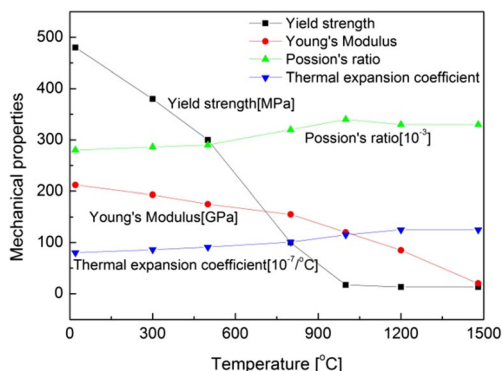

Fig. 6 Temperature-dependent mechanical properties [22]

and their calculation locations. Obviously, the peak temperature of thermal cycle in GMAW is larger than those of the other two test cases at the region far away from weld center. In addition, it can be also found that, at the distance of $D = 5.9$ mm from weld center, the peak temperature of thermal cycle in single-pass hybrid welding is higher than the maximum one (the peak temperature for pass 3) in multi-pass hybrid welding, which are respectively 681 and 645 °C, meaning that the total high temperature area (containing the fusion zone) for single-pass hybrid welding is relatively wider although its weld width is small.

4.2 Analysis of residual stress for single-pass hybrid welding

Figure 10 presents the contours of residual stress component distribution of weldment in single-pass HLAW. From Fig. 10a, it is seen that a large longitudinal tensile residual stress is generated in the weld zone and its vicinity and its peak value is 510 MPa, slightly higher than the yield stress of the base metal of 480 MPa at the room temperature. Compared with longitudinal stress, transverse stress and normal stress along the thickness direction are relatively small. For transverse residual stress, there is a stress contraction near the weld toe. In this study, the corresponding von Mises equivalent stress is also computed, as shown in Fig. 10d. Similar to longitudinal stress component, a high stress concentration is produced in and near the weld zone and the peak value is 506 MPa, slightly greater than the yield stress of base metal. However, the area with higher stress is narrow, demonstrating that there is no serious residual stress in single-pass hybrid welding.

Figure 11 gives the contours of residual stress components and equivalent stress at the cross section of weldment for single-pass hybrid welding. It can be found that the longitudinal and equivalent stresses have a relatively uniform distribution along the thickness direction in the weld zone and its vicinity, but the transverse stress changes largely in this region, which will be discussed in the following section.

Figure 12 provides the residual stress component and equivalent stress distributions in single-pass hybrid welding

Fig. 7 Comparison of the calculated and experimentally measured weld cross sections for **a** case 1, **b** case 2, and **c** case 3
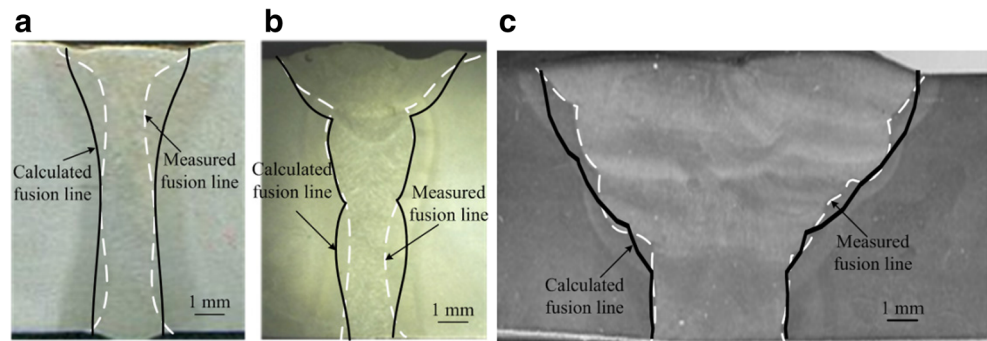
along L1, L2, and L3 defined in Fig. 9a. In Fig. 12a, it is observed that the longitudinal stresses at different thicknesses of weldment have similar distribution features. At the weld zone and surrounding HAZ, large tensile stress is formed and the peak values at different thicknesses are all slightly greater than the yield stress of base metal. With distance from the weld bead, the stress decreases sharply. Due to arc heat input, the area with large stress is slightly wider at the top surface of weldment. As stated above, the transverse stress has a large change along the thickness direction, as shown in Fig. 12b. At the top and bottom surfaces of weldment, the transverse residual stresses have similar distribution trends, for which, a compressive stress is produced at the fusion zone and a tensile stress emerges near weld boundary. However, at the middle part of weld bead ($z = 6$ mm), the opposite case happens. The reason for this phenomenon is probably related to the formation mechanism of residual stress and plate thickness. Transverse stress is correlated to both the longitudinal and transverse shrinkages. When the plate is of large thickness, the temperature distribution and constraint condition vary with thickness to some extent, which has a more obvious effect on transverse stress compared with longitudinal stress. As to normal stress in thickness direction, a compressive stress concentration is located near the weld boundary. Figure 12d shows the corresponding equivalent stresses at different thicknesses. For these three locations, the highest values of equivalent stresses appear near weld center, which are 495, 443, and

478 MPa, respectively. Increasing the distance from weld boundary, they also drop quickly.

4.3 Comparison of residual stresses

Figure 13 compares the longitudinal residual stress distributions for the three cases. It can be seen that, at different thicknesses of weldment, the distribution shapes of longitudinal stress for three cases are similar to each other. However, compared with those of the other two cases, the high stress region in GMAW is obviously wider due to large high temperature zone. For single- and multi-pass hybrid welding, the former has a slightly greater high stress area, especially at the middle part of weldment.

At both the top and bottom surfaces of weldment, the peak values of longitudinal tensile stresses for the three cases are all close to the yield stress of base metal and the ones for multi-pass hybrid welding are slightly higher than those in single-pass hybrid welding and GMAW. Nevertheless, at the middle part of weldment cross section, the peak stress in multi-pass hybrid welding has the smallest value among the three cases, which is only 301 MPa, much lower than the yield stress of base metal. The reason for large change of peak stress with workpiece thickness in multi-pass hybrid welding is due to weld sequence, groove geometry, and welding process feature. Besides, Fig. 13a also compares the calculated longitudinal stresses of the three cases with the corresponding

Fig. 8 Calculated temperature distributions at the cross section of weldment for **a** case 1, **b** case 2 (pass 3), and **c** case 3 (pass 2)
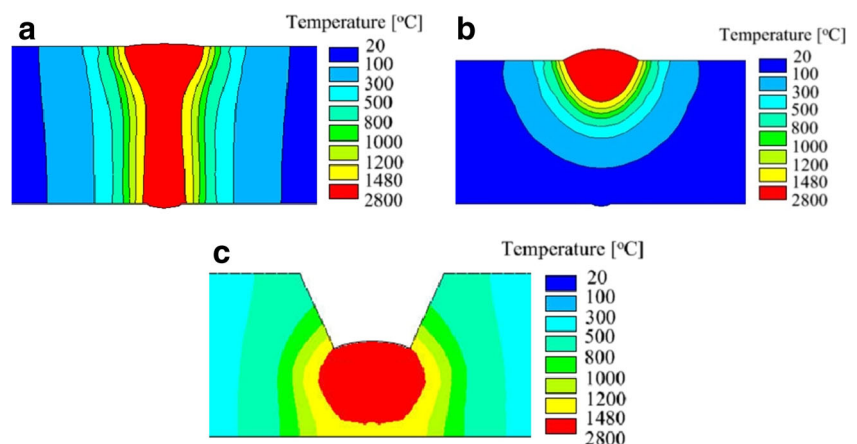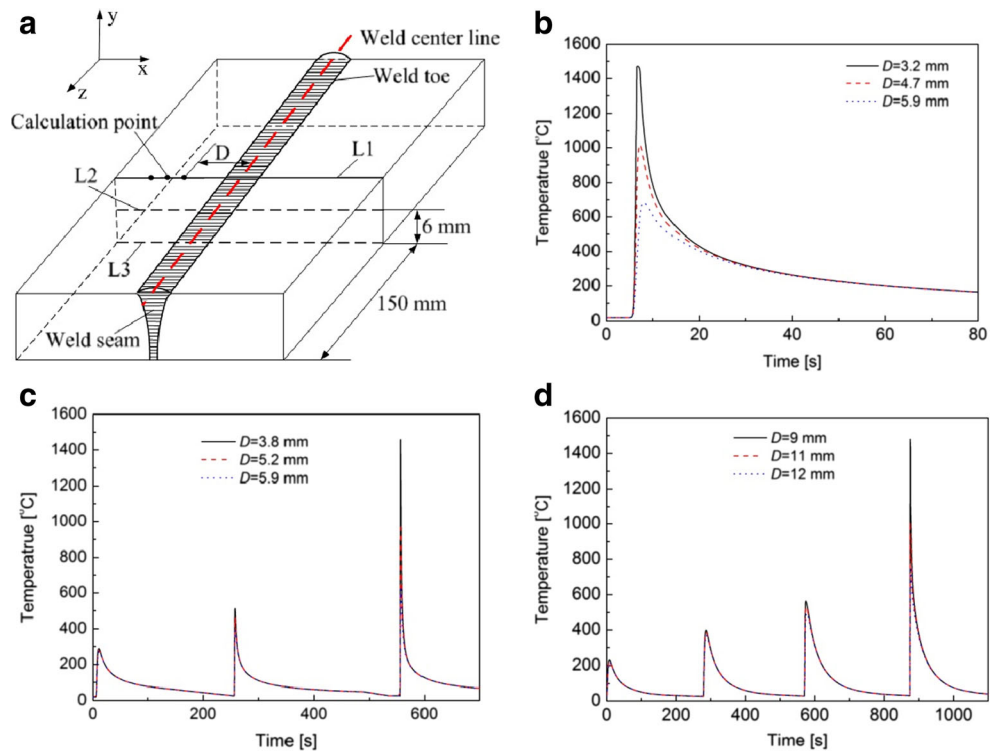
Fig. 9 Schematic of calculation location (**a**) and predicted thermal cycle curves of different points for **b** case 1, **c** case 2, and **d** case 3

measured ones and both are generally in agreement, demonstrating the accuracy of the developed model.

Figure 14 shows a comparison of transverse residual stress distributions for the three cases at different locations. Figure 14a compares the predicted transverse stresses for the three cases with the corresponding measured data, which also have an agreement on the whole. From Fig. 14, it is revealed that, at different thicknesses, the transverse stresses in GMAW still have similar distribution trends to those in single hybrid welding. The former has larger high-stress regions and the latter has slightly higher peak stresses, which are also much less than the yield stress of base metal. However, for multi-pass hybrid welding, its transverse stress distribution is obviously different from those of the other cases. In Fig. 14a, it is seen that, at the top surface of weldment, although the

distribution shape of transverse stress in multi-pass hybrid welding is alike to those in single-pass hybrid welding and GMAW, the peak value of tensile transverse stress is much larger than those of the other two cases. Figure 14b presents the transverse residual stresses along line L2 for three cases. Different from that at the top surface, for single-pass hybrid welding and GMAW, lower tensile transverse stresses are produced in and around the fusion zone. However, for multi-pass hybrid welding, the extremely opposite case occurs. A higher compressive transverse stress can be found at the welding zone and surrounding HAZ; its peak value reaching 315 MPa.

Figure 14c gives the transverse stress distributions at the bottom surface of weldment for the three cases. Contrary to those in single-pass hybrid welding and multi-pass GMAW, a much greater transverse tensile stress appears at the fusion

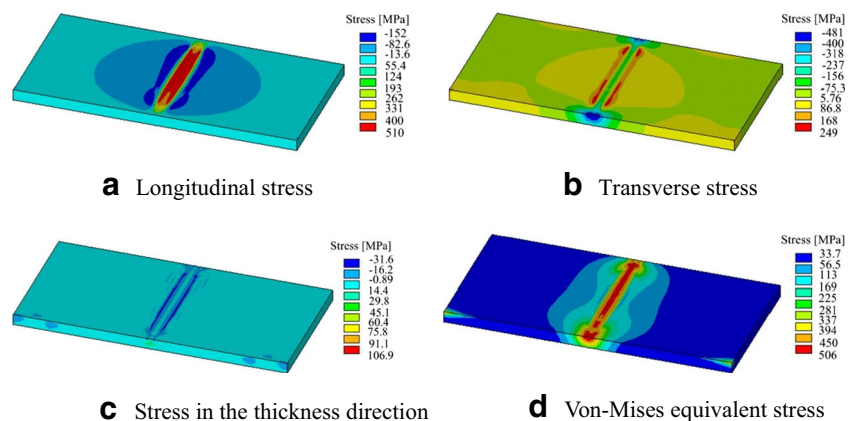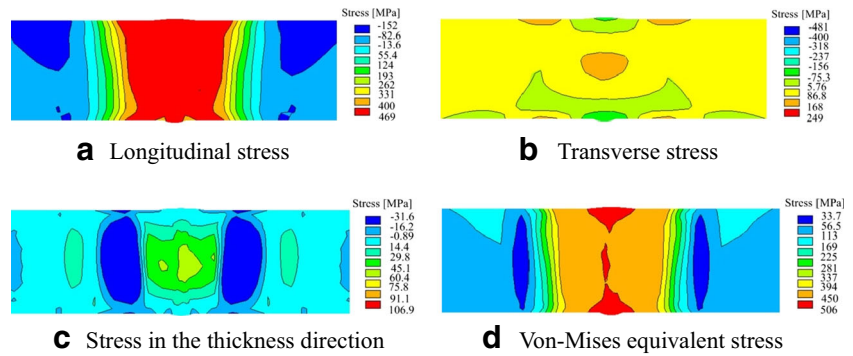**Fig. 10** Contours of residual stress of weldment in single-pass hybrid welding

a Longitudinal stress

b Transverse stress

c Stress in the thickness direction

d Von-Mises equivalent stress

a Longitudinal stress   **b** Transverse stress

c Stress in the thickness direction   **d** Von-Mises equivalent stress

zone in multi-pass hybrid welding and its peak value reaches 412 MPa, obviously higher than that at the top surface of weldment. With the distance increasing from weld boundary, the tensile stress drops largely but no compressive stress emerges. This phenomenon is expected since during multi-pass welding, each weld pass has a bending effect on the weldment due to transverse shrinkage of weld material, which is superimposed at the weld root, thus causing a high transverse tensile stress. For multi-pass hybrid welding, the small weld width at the bottom of weldment further increases its severity.

Figure 15 presents the Von Mises equivalent stresses along lines L1, L2, and L3 for the three cases. It is clearly found that, at different thicknesses of weldment, the von Mises equivalent stresses for the three cases have similar distribution shapes and peak values. In the weld zone and its vicinity, there is little difference in equivalent stress distribution feature between single-pass and multi-pass hybrid welding. Base on the above

analysis, it is seen that, compared to those in GMAW, the region with high stress in hybrid welding is reduced largely, which contributes to the enhancement of welded joint quality. But there is no improvement in peak value of stress, which is not consistent with those of Zhang et al. [14] .

4.4 Comparison of distortion

Figure 16 shows the contours of y-directional displacement (deflection) of the weldment for three cases. Figure 17 presents the calculated deflection distributions along line 1 for three cases. It is seen that, for the three cases, the deflection values are all relatively small. But the vertical deformation in single-pass hybrid welding has the lowest value among the three cases, which is only approximately one sixth of those of the other two cases at the cross section of $z = 150$ mm.

Fig. 12 Residual stress
components and von Mises
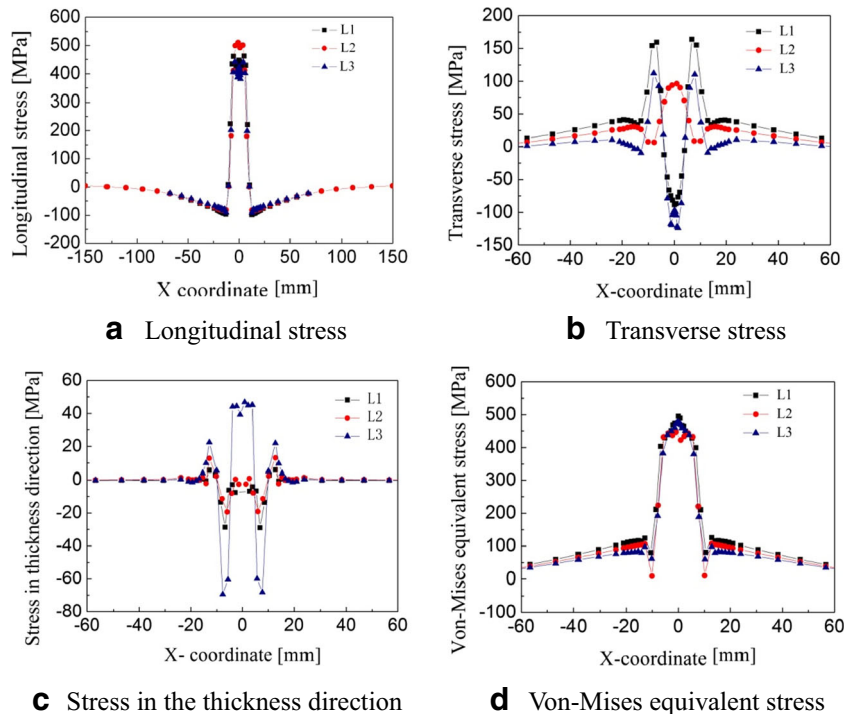equivalent stress along lines L1,
L2, and L3 for case 1

a Longitudinal stress   **b** Transverse stress

c Stress in the thickness direction   **d** Von-Mises equivalent stress

Fig. 13 Longitudinal residual stress distributions along lines L1 (**a**), L2 (**b**), and L3 (**c**) for the three cases
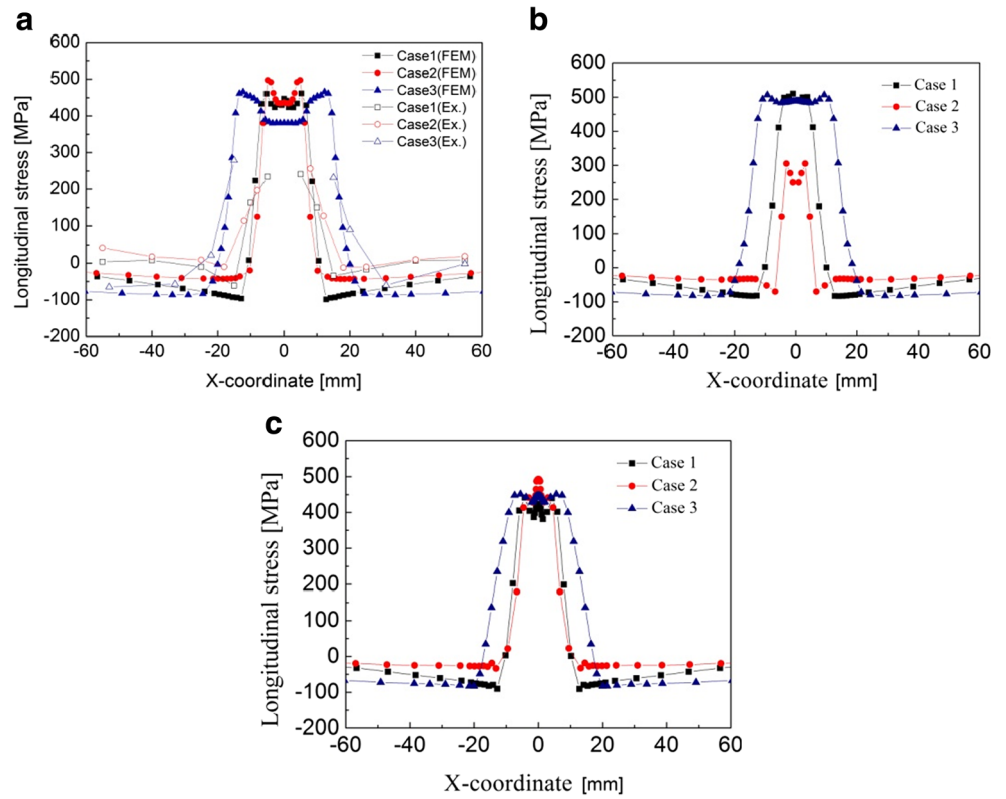

Fig. 14 Transverse residual stress distributions along lines L1 (**a**), L2 (**b**), and L3 (**c**) for the three cases
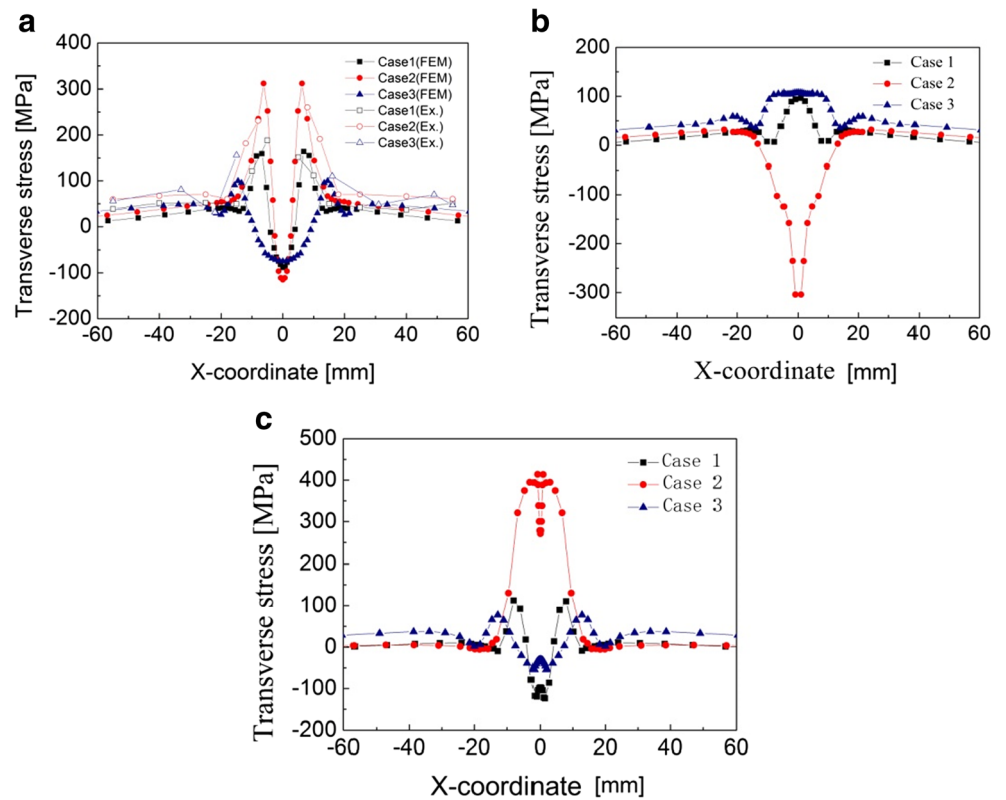
Fig. 15 Von Mises equivalent stress distributions along lines L1 (**a**), L2 (**b**), and L3 (**c**) for the three cases
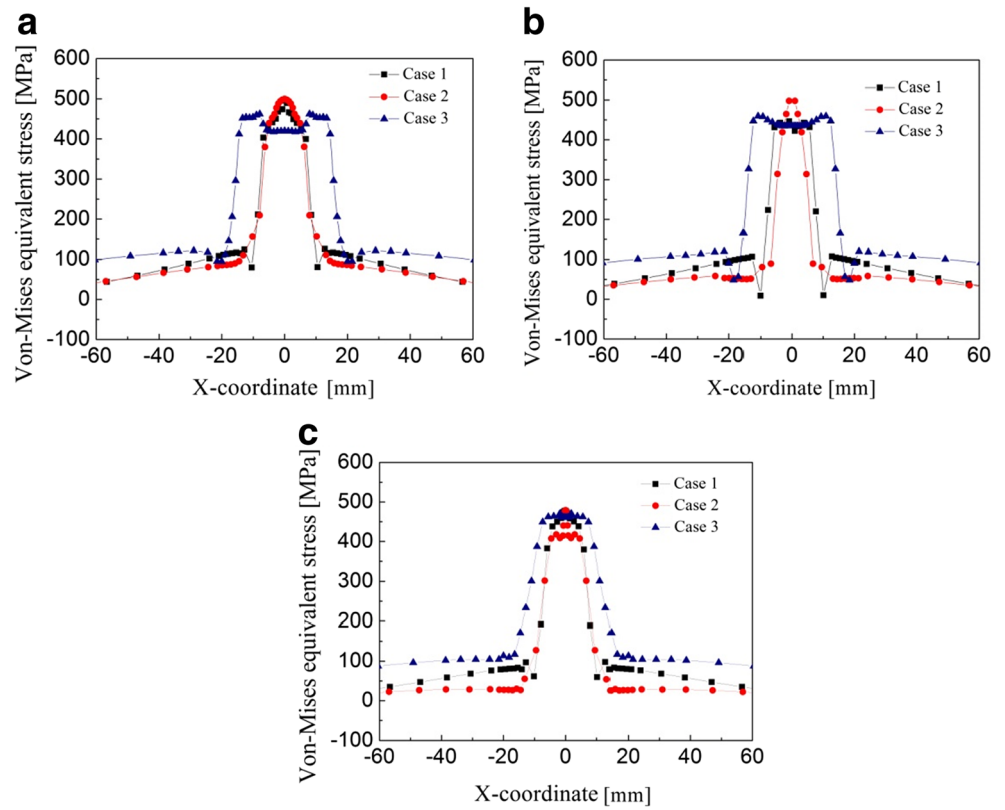

Figure 18 provides the calculated *x*-directional displacements (transverse shrinkage) along lines L1, L2, and L3 for the three cases, respectively. In Fig. 18a, it is indicated that, at different thicknesses, a relatively large transverse displacement in the *x*-direction appears in and near weld metal. In the region slightly far away from weld bead, it drops sharply. Meanwhile, Fig. 18a also shows that there is a small difference in *x*-directional displacement at different thicknesses for single-pass hybrid welding. The reason for this behavior is

that weld width (or temperature field width) changes little in thickness direction. For multi-pass hybrid welding, the transverse displacement distribution feature on bottom surface of weldment is similar to that in single-pass hybrid welding but the ones at the top surface and middle part are close to those in GMAW, as indicated in Fig. 18b and c. A common feature is that with the distance increasing from weld boundary, transverse displacement increases and then retains relatively stable at a high value. However, in multi-pass hybrid welding and
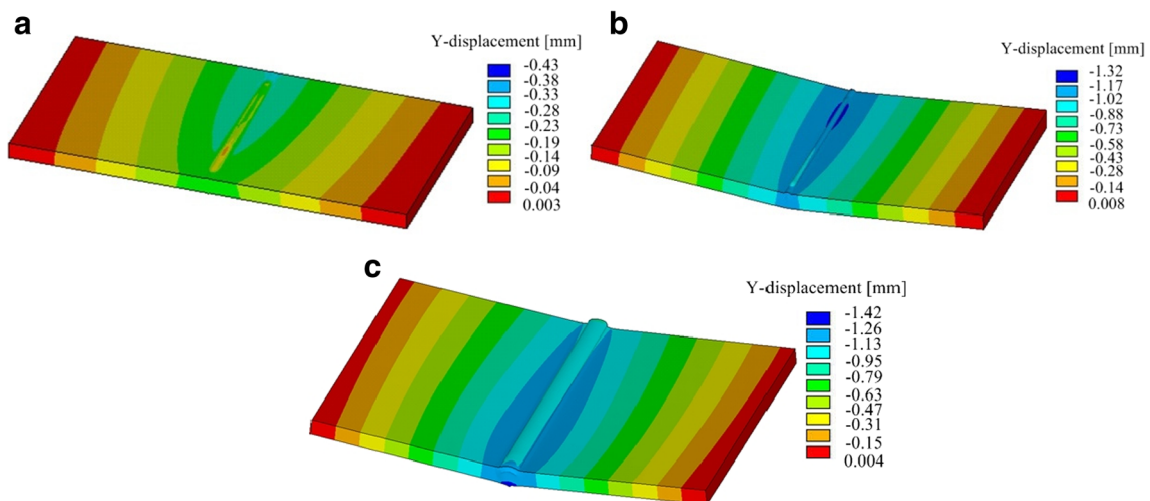

Fig. 16 Contours of *y*-directional displacement for **a** case 1, **b** case 2, and **c** case 3
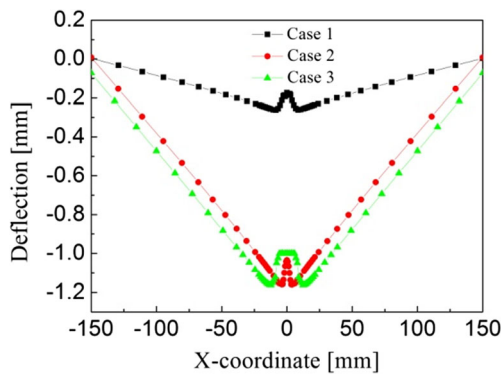
**Fig. 17** Deflection distributions along line L1 for the three cases

GMAW, the weld width has a relatively big variation along the thickness direction of weldment. Thus, for these two cases, the differences in transverse shrinkage between top and bottom surfaces of weldment are obviously higher than that in single-pass hybrid welding, thereby resulting in a relatively great angular deformation. In addition, from Fig. 18, it is also founded that, compared with those in single-pass and multi-pass hybrid welding, a relatively large transverse shrinkage deformation emerges in GMAW due to large transverse displacement at both top and bottom surfaces of weldment. It should be noted that, due to that the deflection and x-directional displacement are very small for three cases, they are not experimentally measured in this study, which will be solved in the future research.

5 Conclusions

1. A three-dimensional finite element model is developed to investigate the residual stress and deformation in HLAW for butt joint of 12-mm-thick Q460 steel. Distribution features of residual stress and distortion under different welding conditions were numerically analyzed.

2. Higher longitudinal tensile stress is located in and near the fusion zone and its peak value is greater than the yield stress of base metal, and the corresponding von Mises equivalent stress has similar distribution. Compared with GMAW, the area with high residual stress in HLAW is much narrower, but there is no any improvement in peak value of residual stress. Moreover, transverse tensile stress at the weld root in multi-pass hybrid welding is much larger than those in single-pass hybrid welding and GMAW.

3. For 12-mm thick Q460 steel, welding distortions for hybrid welding and GMAW are not very serious. The welding distortion in single-pass hybrid welding is much smaller compared with those in multi-pass hybrid welding and GMAW. The latter two cases have the similar angular distortion.

Fig. 18 *x*-Directional displacements along lines L1, L2, and L3 for **a** case 1, **b** case 2, and **c** case 3
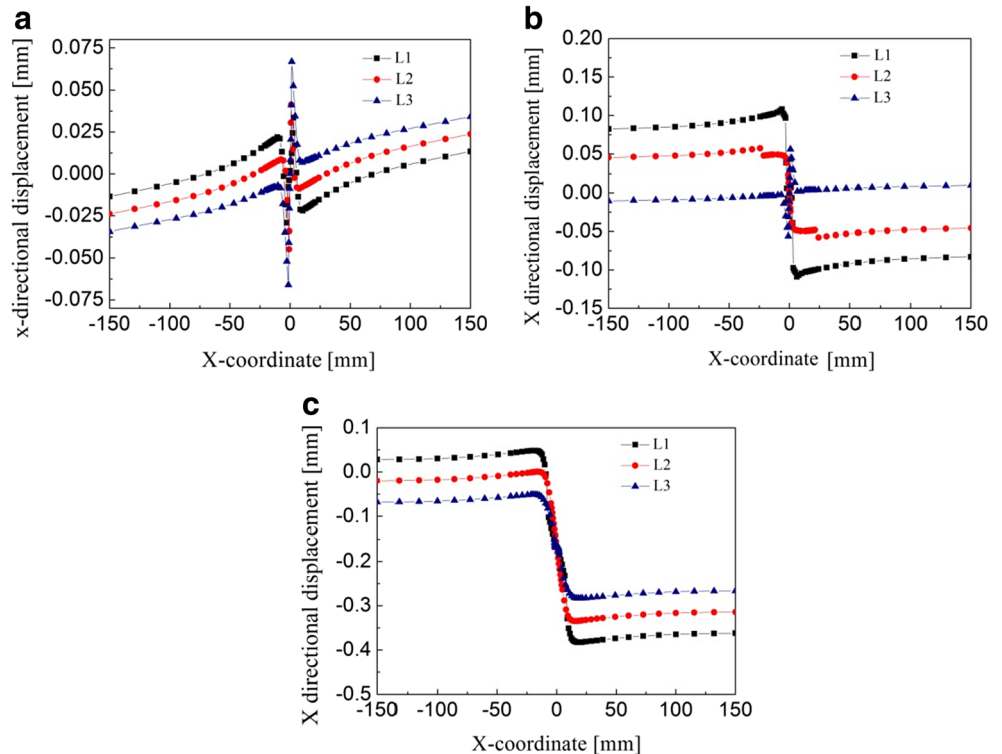
References

1. Staufer H (2007) Laser hybrid welding in the automobile industry. Weld J 86:36–40

2. Defalco J (2007) Practical applications for hybrid laser welding. Weld J 86:47–50

3. Wahha M, Mazutani M, Katayama S (2016) Single pass hybrid laser-arc welding of 25-mm thick square groove butt joints. Mater Des 97:1–6

4. Deng DA (2009) FEM prediction of welding residual stress and distortion in carbon steel considering phase transformation effects. Mater Des 30(2):359–366. https://doi.org/10.1016/j.matdes.2008.04.052

5. Cao X, Wanjara P, Huang J, Munro C, Nolting A (2011) Hybrid fiber laser-arc welding of thick section high strength low alloy steel. Mater Des 32(6):3399–3413. https://doi.org/10.1016/j.matdes.2011.02.002

6. Mazar M, Ma J, Yang G, Kovacevic R (2014) Hybrid laser/arc welding of advanced high strength steel in different butt joint configurations. Mater Des 64:573–587. https://doi.org/10.1016/j.matdes.2014.08.011

7. Mazar M, Ma J, Liu W, Kovacevic R (2015) Pore formation and its mitigation during hybrid laser/arc welding of advanced high strength steel. Mater Des 67:509–521. https://doi.org/10.1016/j.matdes.2014.10.072

8. Cho JH, Na SJ (2009) Three dimensional analysis of molten pool in GMA-laser hybrid welding. Weld J 88:35–43

9. Cho WI, Na SJ, Cho MH, Lee JS (2010) Numerical study of alloying element distribution in CO_2 laser–GMA hybrid welding. Comput Mater Sci 49(4):792–800. https://doi.org/10.1016/j.commatsci.2010.06.025

10. Zhou J, Tsai HL (2008) Modeling of transport phenomena in hybrid laser-MIG keyhole welding. Int J Heat Mass Transf 51(17-18):4353–4366. https://doi.org/10.1016/j.ijheatmasstransfer.2008.02.011

11. Xu GX, Zhang WW, Liu P, Du BS (2015) Numerical analysis of fluid flow in laser + GMAW hybrid welding. Acta Metall Sin 51:713–723

12. Xu GX, Wu CS, Qin GL, Wang XY, Lin SY (2011) Adaptive volumetric heat source models for laser beam and laser + pulsed GMAW hybrid welding processes. Int J Adv Manuf Technol 57(1-4):245–255. https://doi.org/10.1007/s00170-011-3274-x

13. Heinze C, Schwenk C, Rethmeier M (2012) Numerical calculation of residual stress development of multi-pass gas metal arc welding. J Constr Steel Res 72:12–19. https://doi.org/10.1016/j.jcsr.2011.08.011

14. Zhang T, Wu CS, Qin GL, Lin SY (2010) Thermomechanical analysis for laser + GMAW-P hybrid welding process. Comput Mater Sci 47(3):848–856. https://doi.org/10.1016/j.commatsci.2009.11.013

15. Hee SB, Han SB, You CK, Sung MJ (2010) Analysis of residual stress on AH32 butt joint by hybrid CO2 laser-GMA welding. Comput Mater Sci 49:217–221

16. Kong FR, Ma JJ, Kovacevic R (2011) Numerical and experimental study of thermally induced residual stress in the hybrid laser–GMA welding process. J Mater Process Technol 211(6):1102–1111. https://doi.org/10.1016/j.jmatprotec.2011.01.012

17. Xu GX, Wu CS, Ma XZ, Wang XJ (2013) Numerical analysis of welding residual stress and distortion in laser + GMAW hybrid welding of aluminum alloy T-joint. Acta Metall Sin (Engl Lett) 26(3):352–360. https://doi.org/10.1007/s40195-012-0166-5

18. ASTM E837-01 (2001) Standard test method for determining residual stress by the hole drilling strain gage method. Am Soc Test Mater, Philadelphia

19. Xu GX, Wu CS, Qin GL, Wan XY (2012) Finite element analysis of temperature field in laser + GMAW hybrid welding for T-joint of aluminum alloy. Acta Metall Sin 48(9):1033–1041. https://doi.org/10.3724/SP.J.1037.2012.00174

20. Liu C, Luo Y, Yang M, Fu Q (2017) Three-dimensional finite element simulation of welding residual stress in RPV with two J-groove welds. Weld world 61(1):151–160. https://doi.org/10.1007/s40194-016-0392-y

21. Deng DA, Kiyoshima S (2010) FEM prediction of welding residual stress in a SUS304 girth-welded pipe with emphasis on stress distribution near weld start/end location. Comput Mater Sci 50(2):612–621. https://doi.org/10.1016/j.commatsci.2010.09.025

22. Du BS, Ma XZ, Zhang ZW, Xu GX (2014) Numerical simulation of residual stress in multi-pass weld joint of ultra-grained Q460 steel. Trans China Weld Inst 35:42–46